

Complementary magnon transistors by comb-shaped gating currents

Peng Chen,^{1,2,†} Hanchen Wang^{④,3,4,5,‡} Chen Cheng,^{1,‡} Caihua Wan,^{1,2,*} Dalin Zhang,⁶ Yuqiang Wang^{④,1} Yizhan Wang^{④,1} Wenqing He,¹ Boyuan Chi,¹ Yaowen Liu,⁶ Guoqiang Yu,^{1,7} Haiming Yu,^{3,4} and Xiufeng Han^{④,1,2,7,‡}

¹ Beijing National Laboratory for Condensed Matter Physics, Institute of Physics, University of Chinese Academy of Sciences, Chinese Academy of Sciences, Beijing 100190, China

² Center of Materials Science and Optoelectronics Engineering, University of Chinese Academy of Sciences, Beijing 100049, China

³ Fert Beijing Institute, Ministry of Industry and Information Technology Key Laboratory of Spintronics, School of Integrated Circuit Science and Engineering, Beihang University, Beijing 100191, China

⁴ International Quantum Academy, Shenzhen, China

⁵ Department of Materials, ETH Zurich, Zurich 8093, Switzerland

⁶ School of Physics Science and Engineering, Tongji University, Shanghai 200092, China

⁷ Songshan Lake Materials Laboratory, Dongguan, Guangdong 523808, China



(Received 22 February 2023; accepted 11 October 2023; published 8 November 2023)

Complementary magnon transistors (CMTs) are desired to effectively regulate the transport of coherent spin waves. Here, using comb-shaped gating electrodes with a variable duty ratio (δ) and a gating current flowing through them, we were able to decrease or even increase the transmission of spin waves in a wide frequency range complimentarily. The reduction or amplification degree at opposite gating currents depends on δ . We further found that interference between spin waves transmitted through the gated and ungated regions was responsible for the gate tunability at low δ ; at high δ , the inhomogeneous temperature and magnetic fields introduced by the gating currents can nontrivially deflect spin waves and leads to an opposite gate tunability. Realization of the CMT based on a dc gating current may pave the way toward coherent magnon devices and circuits, spin-wave processing, or lensing applications.

DOI: 10.1103/PhysRevApplied.20.054019

I. INTRODUCTION

Complementary metal oxide semiconductor (CMOS) devices have contributed immensely to the success of microelectronics over recent decades because they enable an efficient and complementary mode of control over the electrotransport property of semiconductors. For magnonics (an emerging realm of exploring magnons to store, transmit, and process data) [1–19], a magnon transistor is also being pursued to complementarily regulate magnon transport by an electric gating, akin to the CMOS devices for microelectronics. Several magnon (spin-wave, or SW for short) transistors [1–9] and spin-wave lenses [16–19] have been developed. Cornelissen *et al.* [6] have proposed three Pt stripes as the magnon source, gate, and drain, dispersed in parallel on a $\text{Y}_3\text{Fe}_5\text{O}_{12}$ (yttrium iron garnet, YIG) film. The magnon-mediated current drag effect between the source and the drain is controlled by a current flowing in

the middle gate, which modulates the magnon density in the YIG magnon channel.

Given their advantages over thermal magnons, coherent magnons with an additional degree of freedom (phase) have also been used to design magnon transistors [1,2], one of which is composed of a magnon crystal and three radio-frequency (rf) antennas [1]. The magnon crystal has structure-determined magnon conduction bands and band gaps. The spin waves activated in the frequency of the conduction bands can be effectively transmitted from the source to the drain antennas until evanescent spin waves, the frequencies of which are located in the nearby band gaps, are activated by the gate antenna. The transmitted and evanescent spin waves with different but close frequencies can still interact strongly, which significantly reduces the SW transmission from source to drain by the ac gate current through a magnon scattering process [1]. This magnon transistor thus has an ultrahigh on-off ratio in specific frequency regions; however, its size is in the order of centimeters, hampering its scaling. Recently, the dc gate current, which is more suitable for microelectronics, has also been deployed to control the transport of coherent

*wancaihua@iphy.ac.cn

†xfhan@iphy.ac.cn

‡These authors contributed equally to this work.

magnons. One possible mechanism behind this tunability is the spin Hall effect, which can weaken (enhance) the decay of spin waves by transferring antidampinglike (dampinglike) torques.

Here, using a comb-shaped gate with a variable duty ratio (δ), we demonstrate that the spin-wave transmission in a wide frequency range can be reduced or even amplified by spin-wave interference via a gating current and as-induced inhomogeneous Oersted field distribution and temperature distribution. This complementary magnon transistor (CMT), which is controllable by a dc gate, after fixing the scaling-down issue, may pave the way for the development of coherent magnonic logic devices and circuitry. Moreover, again owing to its complementary gate effect on the coherent spin-wave transmission, this magnon transistor can also be applied in spin-wave processing, an energy-efficient nonconventional data processing architecture. The deflection of spin wave packages controllable by the gate current may also be used to develop spin wave lenses.

II. METHODS

We used magnetron sputtering to grow YIG thin films with a thickness of 50 nm on $\text{Gd}_3\text{Ga}_5\text{O}_{12}$ (GGG) substrate and we then made them into single crystals through high-temperature annealing [20–24]. As shown in Fig. 1(a), a couple of Au microwave antennas (with a thickness of 100 nm, a width of 4.4 μm , and an interval of 80 μm) were patterned on the YIG films by lithography and lift-off processes to excite and detect SWs. They acted as the magnon source and drain, respectively. A series of equally separated comb-shaped Au bars (5 nm thick, 2 μm wide, and 50 μm long) were deposited between the magnon source and drain as a gate for the SW control. Another pair of 5- μm -wide Au bars were fabricated on both ends of the magnon gates to source the dc current and they were 200 nm thick, which was sufficient to unify the current density flowing through each Au bar in the gating region. Afterward, the magnon source and drain were connected to the S_1 and S_2 ports of a vector network analyzer (VNA) (R&S ZVA40). In order to reduce the nonlinear effects of the SW, the excitation power of the VNA was fixed as low as -5 dBm and meanwhile the gate electrodes were connected to a Keithley 2400 dc source.

III. RESULTS AND DISCUSSION

We prepared the device shown in Fig. 1(a) on a 50-nm-thick YIG for detection of the SW. A pair of Au antennas on both sides were connected to two ports of the VNA as, respectively, the excitation port (source) and the detection port (drain) of the SW, and the middle comb-shaped electrode was connected with a dc current source as the control gate of the SW. We mainly studied the transmission parameter S_{21} obtained by the VNA as a function of

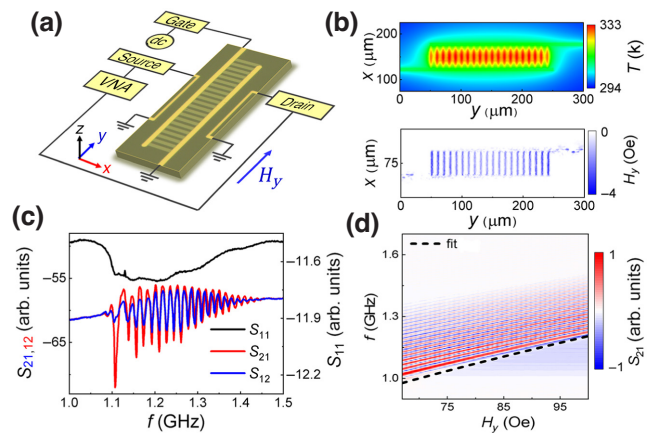


FIG. 1. The experimental setup for the DE-mode SW measurement. (a) A schematic diagram of the magnon transistor device for exciting and detecting the SW. (b) The simulated distributions of the temperature field (above) and the y -directional Oersted field (below) as $\delta = 0.4$. (c) The SW reflectivity and transmission spectra of S_{11} , S_{21} , and S_{12} when $H_y = 80$ Oe. S_{21} has a larger magnitude than S_{12} , a typical nonreciprocal feature for the DE-mode SW. (d) Two-dimensional (f , H_y) mapping of the SW transmission S_{21} . The dotted line in (d) is the fitting curve as $k = 0$.

the gating current. To interpret the SW behavior precisely, we simulated the temperature distribution and magnetic field distribution generated by the gate current via finite-element modeling [Fig. 1(b)]. Except where pointed out, the direction of the applied magnetic field was fixed along the y axis, perpendicular to the wave vector of the SW, to activate a Damon-Eshbach (DE) mode SW [Figs. 1(c) and 1(d)] [25–27]. The oscillations in Fig. 1(c) are induced by the phase delay of the coherent SW during their propagation process. As shown in Fig. 1(d), the phase difference $\Delta\varphi$ between two neighboring peaks is $\Delta\varphi \equiv \Delta k \cdot L_{SD} \equiv 2\pi$, where L_{SD} is the center-to-center distance between the magnon source and drain. Therefore, group velocities v_g as a function of frequency f can be extracted from Fig. 1(d) by using Eq. (1) (see Appendix A) [26,28]:

$$v_g = \Delta f \cdot L_{SD}, \quad (1)$$

where Δf is the frequency difference between neighboring peaks and the frequency of each point is assumed to be the frequency center of two neighboring peaks by approximation. The v_g of the SW is the derivative of the frequency with respect to the wave vector k , which can be described as follows [25,29]:

$$f = \frac{\mu_0 |\gamma|}{2\pi} \left[\left(H_y + \frac{2A}{\mu_0 M_s} k^2 \right) \left(H_y + M_s + \frac{2A}{\mu_0 M_s} k^2 \right) + \frac{M_s^2}{4} (1 - e^{-2kt}) \right]^{\frac{1}{2}}, \quad (2)$$

$$v_g = \frac{2\pi df}{dk}, \quad (3)$$

where $|\gamma|$ is the gyromagnetic ratio, $A = 3.75 \times 10^{-12}$ J/m is the exchange-stiffness constant of YIG, $\mu_0 M_S$ is the saturation magnetization of YIG, and t is the thickness of the YIG film. Therefore, by using Eq. (3), we can fit the relationship between v_g and f (see Appendix A) to estimate the $\mu_0 M_S$ of YIG, which is about 175 mT. After estimating the material parameters, we replotted the SW frequency as a function of the external magnetic field with a k value of zero, as shown by the black dashed curve in Fig. 1(d), which closely matches with the experiment and also confirms the estimated parameters.

We placed the magnon transistor in a uniform external field H_y , the direction of which was along the y axis, and then picked up the S_{21} signal from the VNA when $I_g = \pm 30$ mA was applied through the gate bars. Figure 2(a) shows that in the S_{21} versus f spectra, there was a red shift (blue shift) of about 3 MHz at $I_g = -30$ mA (+30 mA). We attribute these shifts to the Oersted field (H_I) generated by the gating current superposed on the external field H_y . In Fig. 2(a), we have already offset the S_{21} spectra to align their oscillation peaks to compensate the trivial influence of H_I , as clearly indicated by the x labels of Fig. 2(a). Then, it could be clearly observed that the amplitude of S_{21} became larger at the negative I_g for the f range 0.9–1.7 GHz. To quantitatively describe the gating degree of I_g on the total power (P_{21}) transmitted by the SW, we integrate $|S_{21}|^2$ over f :

$$P_{21}(I_g) = \int S_{21}^2(I_g, f) df. \quad (4)$$

Figure 2(b) shows the I_g dependence of the transmitted SW power in the form of $P_{21}(I_g)$. P_{21} is always stronger at $-I_g$ than at $+I_g$ for this sample. As $+I_g$ is increased, P_{21} decreases monotonously; however, as $-I_g$ is increased, P_{21} first increases and then eventually decreases.

In order to balance the temperature change induced by $\pm I_g$, it is more reasonable to define and use the power-modulation ratio (PMR):

$$\text{PMR} = \frac{\Delta P_{21}(|I_g|)}{P_{21}(-I_g) + P_{21}(+I_g)} = \frac{P_{21}(-I_g) - P_{21}(+I_g)}{P_{21}(-I_g) + P_{21}(+I_g)}. \quad (5)$$

This dependence of P_{21} on I_g is interpreted by the interference effect between spin waves transmitted under gated and ungated regions, as explicitly explained as explicitly explained later. In short, at a negative (positive) gate current, the interference effect enhances (suppresses) the transmission efficiency of spin waves. This leads to the observation that the S_{21} under a negative in Fig. 2(b)

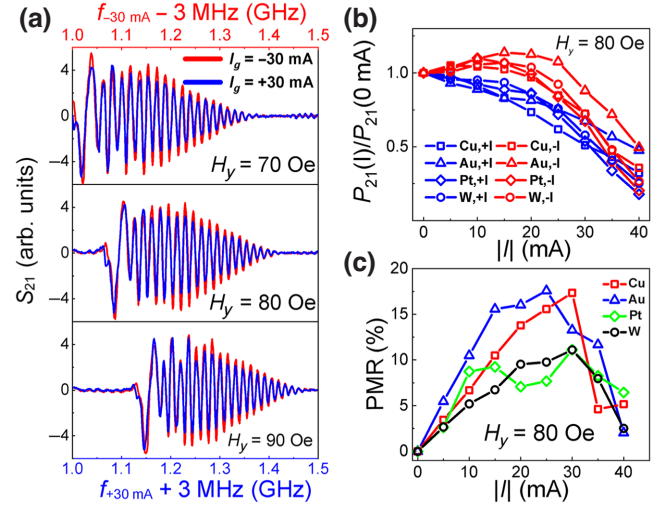


FIG. 2. The modulation of the SW transmission by the gate current. (a) S_{21} SW transmission spectra at different external magnetic fields when the gate current $I_g = -30$ mA (red line) and $I_g = +30$ mA (blue line). The red (blue) line corresponds to the upper (lower) horizontal axis, which has been shifted appropriately in frequency to align the corresponding oscillation peaks in the S_{21} spectra. The shifted frequency is of the order of several megahertz, depending on the magnitude of the gating current. (b),(c) The spin-wave (b) $P_{21}(I)/P_{21}(0)$ value and (c) PMR value when the gate is made of different metals.

increases first but it monotonically decreases under a positive gate current. However, as the gate current increases, the Joule-heating effect brought about by the gate current becomes significant, which greatly increases the magnon-magnon scattering and destroys the interference effect. Thus, both S_{21} and the positive PMR value decrease remarkably as $I_g \geq 30$ mA.

Which reflects the signal change by $\pm I_g$ after canceling out the trivial temperature issue. The PMR also increases initially, reaches a maximum at around 20 mA, and finally decreases to zero at 40 mA with elevating $|I_g|$ [Fig. 2(c)].

It has been reported that the dampinglike spin torque produced by the spin Hall effect (SHE) in heavy metals can be used to suppress or enhance SW decay. In order to identify the physics behind the observed I_g controllability, we measured the S_{21} spectra under the same conditions but for magnon transistors with differing gate materials, Pt, W, Cu, and Au, with positive, negative, negligibly small, and moderately positive spin Hall angles, respectively. The four devices exhibited similar I_g tunability, ruling out any SHE possibilities in our case.

Then, to study the geometric effect of the gate electrodes, we changed the width (w_{Au}) of the Au strips but fixed the periodicity at 10 μm . Here, we have defined the duty ratio $\delta \equiv w_{\text{Au}}/10$. We also kept the current density in the Au strips and other configurations unchanged and measured the S_{21} spectra. First, with increasing

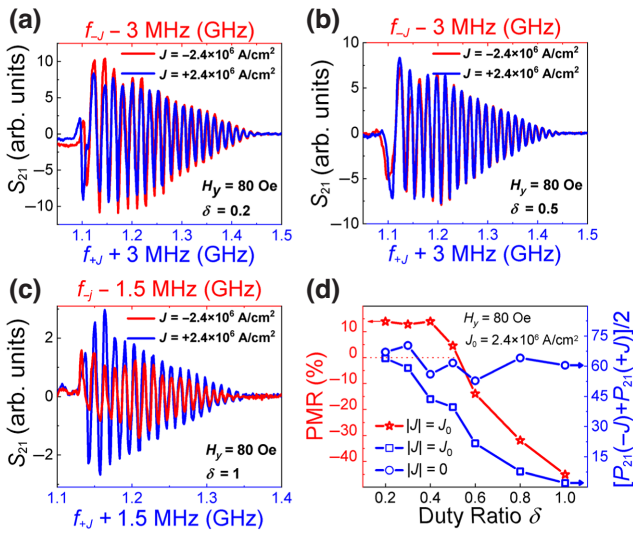


FIG. 3. The SW transmission spectra of magnon transistors with different values of δ . (a)–(c) The S_{21} spectra when δ is (a) 0.2, (b) 0.5, and (c) 1.0, respectively, keeping the gate current density unchanged. (d) The PMR value (red line) and the variation of the total spin-wave intensity $P_{21}(-J) + P_{21}(+J)$ (blue lines) with different values of δ .

δ , $P_{21}(-I_g) + P_{21}(+I_g)$ decreases gradually because the same current density in the larger- δ devices generates more heat, which leads to more magnon-magnon scattering (Appendices B and C). More interestingly, Figs. 3(a)–3(c) show that $\Delta P_{21}(|I_g|)$ changes sign with a varying δ . When $\delta < 0.5$, $\Delta P_{21}(|I_g|) > 0$ and the maximum PMR approach 13%; as $\delta \geq 0.5$, $\Delta P_{21}(|I_g|)$ is negatively reversed [Fig. 3(d)].

It is worth pointing out that the PMR value actually reflects the magnification of the transmitted SW power controlled by I_g after removing the trivial influences from the temperature and H_I . By comparing $P_{21}(-I_g)$ with $P_{21}(+I_g)$ in the PMR ratio, we have compensated the influence of Joule heating, since $\pm I_g$ leads to the same temperature rise for the device. By integrating the transmitted power in the whole frequency range, we have canceled out the trivial influence from the current-induced Oersted field, since this field only leads to a frequency shift in the transmission spectra, as shown in Fig. 2(a). This is the reason why we have defined the PMR parameter to characterize the influence of the gate. Certainly, this CMT can also work in a mode with a fixed frequency. In this case, the frequency shift caused by the gating current has to be taken into account and a huge and frequency-specific gate tunability in S_{21} can be expected, as hinted in Fig. 2(a). Here, in order to realize wide-band control of the spin waves, we still prefer the PMR defined in Eqs. (4) and (5) as a benchmark to show the gate tunability.

The reversible $\Delta P_{21}(|I_g|)$ enables us to realize a complementary control on the SW transmission by controlling

the duty ratio δ . In CMOS devices, the complementarity is achieved by opposite doping types; here, by just patterning gate electrodes with different duty ratios on the same SW channel (YIG), we can realize the complementarity, the opposite gating tunability. For example, $P_{21}(-I_g) > P_{21}(+I_g)$ as $\delta < 0.5$ and the opposite is true as $\delta > 0.5$. If we set the $P_{21}(+I_g)$ as a baseline, the transmitted SW power can be amplified at the corresponding negative gate $-I_g$ in CMTs with $\delta < 0.5$. Certainly, this amplification depends on the baseline definition. If we reselect $P_{21}(-I_g)$ as the baseline, SW amplification can be achieved at $+I_g$ for the CMTs with $\delta > 0.5$. Due to the complementarity, SW power amplification can already be targeted in CMTs with a proper δ gate once the baseline is predetermined. This SW amplification and modulation capability is one advantage of this kind of CMT.

To explain the above phenomena, we first consider the case of zero gating current. A spin-wave packet is transmitted from the source to the drain and its phase factor is

$$\Phi_0 = k_0 L_{SD}, \quad (6)$$

where k_0 is the wave vector of a DE SW with frequency f_0 and L_{SD} is the center-to-center distance between the magnon source and the drain. k_0 is related to f_0 as follows:

$$f_0 = \sqrt{\left(f_H + \frac{f_M}{2}\right)^2 - e^{-2k_0 d} \left(\frac{f_M}{2}\right)^2}, \quad (7)$$

$$k_0 = -\frac{1}{2d} \ln \left[\frac{\left(f_H + \frac{f_M}{2}\right)^2 - e^{-2k_0 d} \left(\frac{f_M}{2}\right)^2}{\left(\frac{f_M}{2}\right)^2} \right], \quad (8)$$

Here, $f_H = \gamma H_y$ and $f_M = 4\pi\gamma M_s$. Since we are mainly interested in SWs with small k values here, the exchange interaction can be ignored. Therefore, the dispersion in Eq. (2) can be simplified to that shown in Eq. (7). To scale down to submicrometer devices, magnon transistors that can control spin waves of shorter wavelengths have to be developed. In that case, the exchange interaction cannot be ignored, which is beyond the scope of this paper.

Under the gate regions and after applying I_g , the dispersion shown in Eq. (7) changes, which changes the wave vector k of the SW in the frequency of f_0 according to Eq. (9). Here, the spin-wave frequency f_0 is maintained:

$$f_0 = \sqrt{\left[f_H \pm f_{H_I} + \frac{(f_M - f_{\Delta M})}{2}\right]^2 - e^{-2kd} \left[\frac{(f_M - f_{\Delta M})}{2}\right]^2}, \quad (9)$$

where $f_{H_I} = \gamma H_I$, $f_{\Delta M} = 4\pi\gamma\Delta M$, H_I is the Oersted field, and ΔM is the magnetization reduction caused by the temperature rise. Thus, the SW in the f_0 frequency underneath

the gated regions has a new wave vector k :

$$k = -\frac{1}{2d} \ln \left\{ \frac{\left[f_H \pm f_{H_I} + \frac{(f_M - f_{\Delta M})}{2} \right]^2 - f_0^2}{\left[\frac{(f_M - f_{\Delta M})}{2} \right]^2} \right\}. \quad (10)$$

The SW phase without a gate is still $\Phi_0 = k_0 L_{SD}$. However, in stark contrast, the new SW phase underneath the gated stripes takes the form of Eq. (11) after applying the gate current because the wavevector underneath the gate has been changed as k instead of k_0 . Outside the gate region, the wavevector of spin waves is still k_0 .

$$\begin{aligned} \Phi &= k_0(L_{SD} - L_G) + kL_G = k_0(L_{SD} - L_G) + (k_0 + \Delta k)L_G \\ &= \Phi_0 + \Delta kL_G. \end{aligned} \quad (11)$$

Considering δ , the average SW should thus be contributed by the above two SWs of different wave vectors with δ -related weights and the detected SW amplitude follows

$$\begin{aligned} A &= (1 - \delta) \cos(\Phi_0) + \delta \cos(\Phi) = A_I \cos(\Phi_0 + \Psi), \\ A_I &= \sqrt{[(1 - \delta) + \delta \cos(\Delta kL_G)]^2 + [\delta \sin(\Delta kL_G)]^2}, \\ \sin \Psi &= \frac{\delta \sin(\Delta kL_G)}{\sqrt{[(1 - \delta) + \delta \cos(\Delta kL_G)]^2 + [\delta \sin(\Delta kL_G)]^2}}, \\ \cos \Psi &= \frac{(1 - \delta) + \delta \cos(\Delta kL_G)}{\sqrt{[(1 - \delta) + \delta \cos(\Delta kL_G)]^2 + [\delta \sin(\Delta kL_G)]^2}}. \end{aligned} \quad (12)$$

The intensity of the SW signal received by the drain can thus be expressed as

$$\begin{aligned} P_{21}(I_g) &= \int_{f_{0_{\min}}}^{f_{0_{\max}}} P_{\text{source}} |A|^2 df \\ &\quad \left(f_{0_{\min}} = \sqrt{f_H(f_H + f_M)}, f_{0_{\max}} = f_H + \frac{f_M}{2} \right). \end{aligned} \quad (13)$$

We plot the calculated PMR results in Figs. 4(a) and 4(b). It is notable that the predicted polarity of the I_g -modulation effect is consistent with experiment [PMR > 0 , as shown in Fig. 3(d)] when δ is small. According to the above model, we calculate the PMR $\approx 11\%$ as $\delta = 0.44$, close to the experimental PMR = 13%.

Although the above SW-interference model can account for the experimentally positive PMR sign at small $\delta < 0.5$, it cannot explain the phenomenon of reversed I_g controllability on PMR at larger δ . We speculate that one possible reason is that the above model only considers the SWs propagating along the x axis. In fact, a spin-wave package can have group velocities in both the x and the y directions.

To explain the reversed I_g -gating ability, we consider the actual propagating paths of SW packages. Following

the method in Ref. [25,30], we calculate the isofrequency curves at $f = 1.2$ GHz for various values of T and H_I . According to Ref. [30], a spatial translational symmetry is maintained in the normal direction of the temperature gradient (∇T), while the symmetry is broken along the ∇T direction. When a spin-wave package enters an area where $\nabla T \neq 0$, therefore, its wave-vector component in the direction perpendicular to ∇T remains conserved; instead, the component collinear to ∇T varies. This inevitably leads to deflection of a propagating SW package by a nonuniform T field. For the DE mode in which we are interested here, phenomenologically, SW packages incline to escape from high- T regions. According to the above rules, we can predict the trajectory of SW packets in the isofrequency curves. Besides, we have also simulated the T - and H_I -field distributions introduced by I_g . Combining the above two data sets, we have been able to visualize the actual propagation paths of SW packages. An example is shown in Figs. 4(c) and 4(d). The specific method is explained in Appendix B. Notably, when only the T field is considered, SW packages will propagate away from the high- T region [the black line in Fig. 4(d)]. Further considering the influence of the Oersted field, we find that $-H_I$ ($+H_I$) will cause the SW package to deflect to a higher (lower) degree, as indicated by the red (blue) line in Figs. 4(c) and 4(d).

In order to further confirm this effect, we have activated 100 incident spin-wave packages at the source with their injection locations uniformly distributed and then simulated their propagation paths following the above protocol. The simulation results are shown in Fig. 4(e). Clearly, the red (blue) lines are deflected more strongly (less strongly) than the black lines. In experiment, the signal that we received at the magnon drain was actually the x component of the SW (or the oscillating magnetization of YIG along the x axis at the position of the drain), so in Fig. 4(e), the blue lines at $+H_I$ transmit a higher SW power than the red lines at $-H_I$. In this sense, we have attributed the reversed I_g -gating ability at higher δ [PMR < 0 in Fig. 3(d)] to the different degrees of deflection by the nonuniform T field at opposite H_I fields. Then, we have integrated the x component of the simulated SW under the three conditions and the calculated PMR $\approx -5\%$, which is nearly one order of magnitude less than the experimental values in Fig. 3(d) at most. Note that here we can only integrate the power transmitted by the SW but in reality the phases of SWs deflected to different degrees will also differ and the interference effect among spin-wave packages in their propagation process can be even more complicated. The latter factors will further dephase the SWs, reduce the transmitted power due to the interference, and probably increase the PMR magnitude. However, this interference factor, which can be responsible for the lower |PMR| value than found in experiment, cannot currently be taken into account in our toy model.

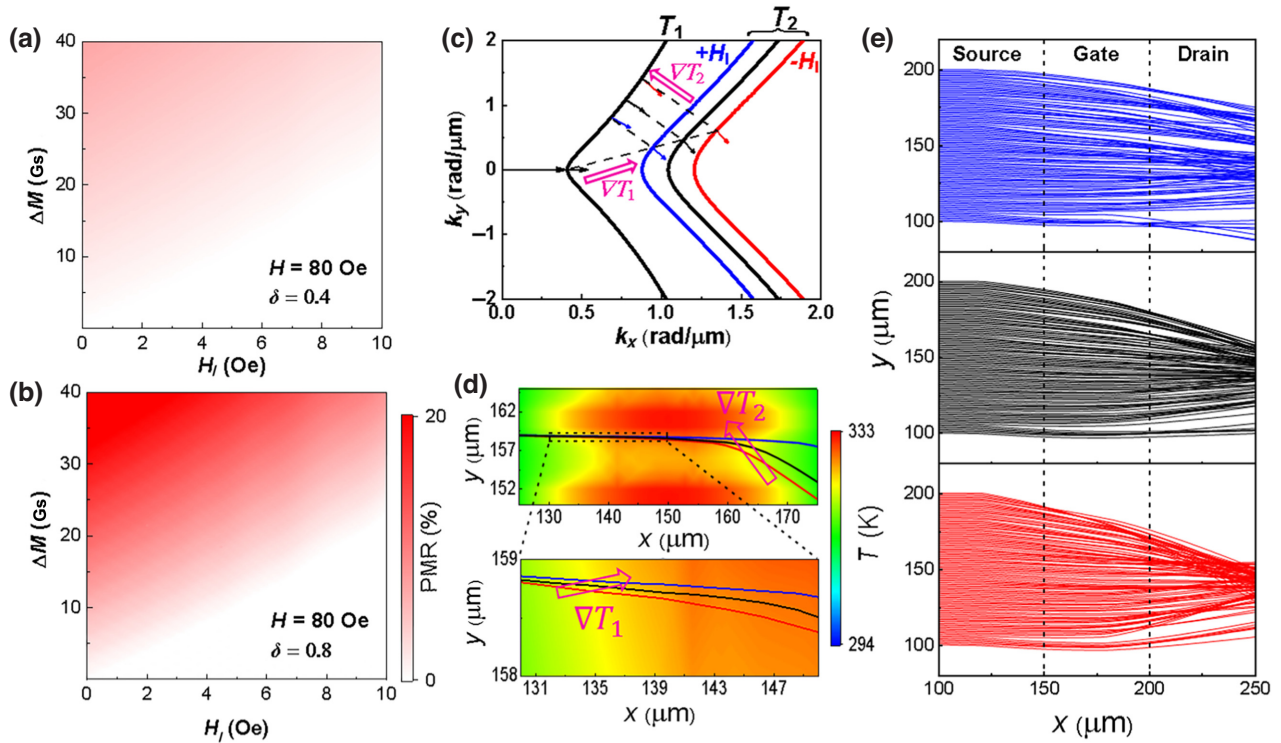


FIG. 4. The theoretical simulation of spin-wave transmission modulated by the gate current. (a),(b) The calculated PMR as a function of ΔM and H_I according to the spin-wave interference model with (a) $\delta = 0.4$ and (b) $\delta = 0.8$. (c) The isofrequency curves under different T and H_I values for $f = 1.2$ GHz, $T_1 = 300$ K, $T_2 = 330$ K, $H_I = 5$ Oe; ∇T_1 and ∇T_2 represent the direction of the temperature gradient sensed by SW packets at the corresponding positions in (d). (d) The propagation paths of the spin-wave packets. The background shows the simulation results of the T distribution. The black line is the propagation path without H_I and the blue (red) line is the propagation path with $+(-)H_I$. (e) The propagation paths of 100 spin-wave packets. In the top (middle) [bottom] figure, a positive (no) [a negative] H_I is taken into account and the same T distribution is used.

Although our CMT has realized complementary control of the spin-wave transmission by a gate current via various values of δ , it has to be engineered toward a smaller size and higher PMR values for practical use. To achieve this goal, smaller transistors hosting exchange-coupled spin waves with shorter wavelengths are desired. Even for the dipolar spin waves that we are currently controlling, there is still plenty of scope to increase the PMR values of our magnon transistors by enhancing the Oersted field and meanwhile constraining the heating effect. For example, the use of materials with a higher conductivity or a greater thickness can be a way to achieve this goal.

IV. CONCLUSIONS

In summary, we have demonstrated a coherent magnon transistor based on a series of comb-shaped gating electrodes with a variable duty ratio δ . At low $\delta < 0.5$, owing to the interference between spin waves in gated and ungated regions, the transmitted SW power at a negative gate current has a larger value than that at a positive gate current. In contrast, when $\delta > 0.5$, the comb-shaped electrodes and the gating current flowing through them

could introduce inhomogeneous temperature and field distributions in the gate region, which deflect the SWs more severely at negative current than at positive current. Therefore, a higher SW power is transmitted at positive current than at negative current, resulting in an opposite gate-current tunability compared with the case of $\delta < 0.5$. This complimentary magnon transistor could provide a valuable perspective for the development of spin-wave processors, spin-wave lenses, and other magnonic devices.

ACKNOWLEDGMENTS

This work was financially supported by the National Key Research and Development Program of China through Ministry of Science and Technology (MOST) Grant No. 2022YFA1402800 and by the National Natural Science Foundation of China (NSFC) through Grant No. 51831012, 12134017] and partially supported by the Strategic Priority Research Program (B) of the Chinese Academy of Sciences (CAS) through Grant No. XDB33000000 and the Youth Innovation Promotion Association of CAS (Grant No. 2020008). H.W. acknowledges the support of the China Scholarship Council (CSC, Grant No. 202206020091).

APPENDIX A: THE GROUP VELOCITIES AS A FUNCTION OF THE FREQUENCY

We use the theoretical dipole-exchange spin-wave dispersion to fit the extracted group velocities as a function of spin wave frequencies. As shown in Fig. 1(d), we can extract the group velocities by using Eq. (1), where Δf is the frequency difference between neighboring peaks and the frequency of each point is assumed to be the frequency center of two neighboring peaks by approximation. The extracted group velocities as a function of the frequencies at 100 Oe is presented in Fig. 5(a). We find that the group velocities decrease with increasing frequencies, which indicates that the measured propagating spin waves are in the dipolar-dominant regime, in the DE configuration. By using Eqs. (2) and (3), we can nicely reproduce the relationship between them [the red curve in the Fig. 5(a)]. From this fit, we can determine that the thickness of the measured YIG film is 50 nm, the saturation magnetization is 175 mT, and the exchange-stiffness constant that we use is 3.75×10^{-12} J/m.

APPENDIX B: METHOD FOR CALCULATING THE PROPAGATION PATH OF SPIN WAVE PACKETS

In this appendix, we provide the parameters for calculating the propagation paths of SW packages. We first simulate the temperature distribution and Oersted-field distribution when a current is applied to the comb-shaped electrode and then calculate propagation paths of the SW packets. The steps in the calculation are as follows:

(1) We set the activation position of the SW packets at $x = 100 \mu\text{m}$, which corresponds to the position of the source antenna of the magnon transistor, and initialize the direction of the group velocity (v_{g0}) of the SW along the $+x$ direction. Meanwhile, the temperature and magnetic

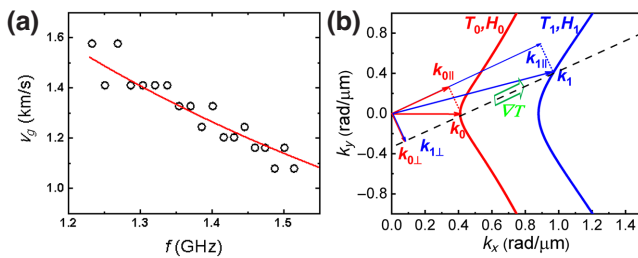


FIG. 5. (a) The spin-wave group velocities as a function of the frequencies extracted from the spectra in the line plot. The red curve is the theoretical fit by using Eqs. (2) and (3). (b) The isofrequency curves of the DE spin waves at (T_0, H_0) and (T_1, H_1) . The black dotted line is the direction of the temperature gradient (∇T). The red and blue arrows are the directions of the incident and scattered wave vectors at (T_0, H_0) and (T_1, H_1) , respectively.

field distributions at different places can be obtained from the finite-element modeling and the isofrequency curves at this time can be determined by using Eq. (2), as shown in Fig. 5(b). The wave vector of the considered SW can be obtained from the isofrequency curves. Using the method in Appendix A, the group velocity (v_{g0}) of the SW packet can be calculated.

(2) Then, we give the considered SW packet a small time step ($\Delta t = 1 \mu\text{s}$ used here) to move forward, during which we assume that the group velocity of the SW remains unchanged until it reaches a new location after the time interval. We can then obtain the new spatial coordinates of the SW packet.

(3) We iterate step (1) at the new location: we update a new temperature gradient and a Oersted field at the new location and recalculate the isofrequency curves in this case. Due to the updated temperature gradient, (i) the wave-vector component perpendicular to the new temperature gradient remains conserved and (ii) the component collinear to the temperature gradient varies. As shown in Fig. 5(b), the wave-vector component $k_{0\perp}$ perpendicular to k_0 remains unchanged, $k_{0\perp} = k_{1\perp}$. The wave-vector component $k_{0\parallel}$ parallel to k_0 changes gradually, $k_{0\parallel} \rightarrow k_{1\parallel}$. Because the temperature gradient and magnetic field sensed by the SW packet change from (T_0, H_0) to (T_1, H_1) and the wave vector of the SW packet changes from k_0 to k_1 , the new group velocity v_{g1} corresponding to k_1 can be calculated from Appendix A.

(4) The obtained v_{g1} is used to iterate propagation of the SW packet at the next time step and steps (2) and (3) are repeated. The iteration is stopped when the SW packet arrives at the drain antenna at $x = 250 \mu\text{m}$.

At this point, we finally obtain a trajectory of the considered propagating SW packet.

APPENDIX C: SIMULATION RESULTS OF SPIN-WAVE PROPAGATION TRAJECTORIES UNDER DIFFERENT DUTY RATIOS

We have calculated the spin-wave propagation-path diagrams for duty ratios $\delta = 0.2, 0.4, 0.6$, and 0.8 , and for $J = \pm 2.4 \times 10^6 \text{ A/cm}^2$, as shown in Fig. 6. When $\delta = 0.2$, the spin-wave propagation path does not change significantly when applying positive or negative current and the spin-wave transmission efficiency is mainly modulated by the interference effect, as described by Eqs. (11)–(13). As the duty ratio δ increases (e.g., $\delta = 0.6$ or 0.8), the spin-wave propagation direction is gradually deflected when $J = -2.4 \times 10^6 \text{ A/cm}^2$ (top panel), leading to notable energy loss and a lower transmission efficiency during the propagation process. In stark contrast, the spin-wave propagation path appears to still be straight (or not severely deflected) and the transmission efficiency remains high

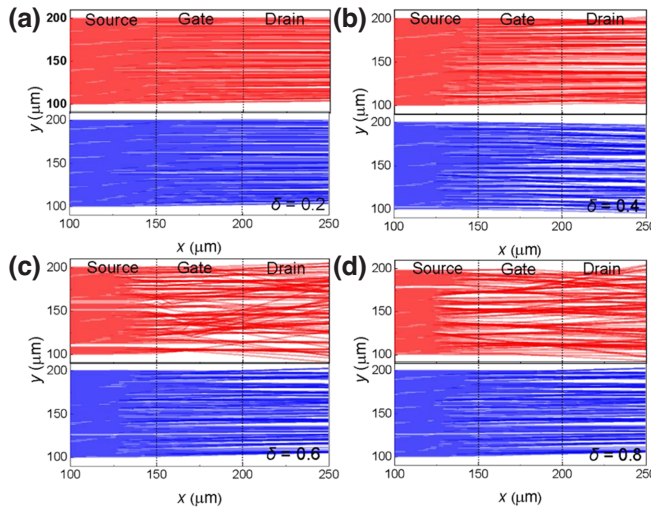


FIG. 6. Simulation diagrams showing the propagation paths of spin waves under different duty ratios. (a)–(d) The path diagrams for duty ratios of δ = (a) 0.2, (b) 0.4, (c) 0.6, and (d) 0.8, respectively. The red lines in the upper panels (blue lines in the lower panels) indicate the path diagrams when applying a negative (positive) current in the gate electrode.

when $J = +2.4 \times 10^6 \text{ A/cm}^2$ (bottom panel), thus leading to a negative PMR value that is qualitatively consistent with the experimental results.

- [1] A. Chumak, A. V. Serga, and B. A. Hillebrands, Magnon transistor for all-magnon data processing, *Nat. Commun.* **5**, 5700 (2014).
- [2] A. V. Chumak, V. I. Vasyuchka, A. A. Serga, M. P. Kostylev, V. S. Tiberkevich, and B. Hillebrands, Storage-recovery phenomenon in magnonic crystal, *Phys. Rev. Lett.* **108**, 257207 (2012).
- [3] M. S. Sarker, H. Yamahara, and H. Tabata, Current-controlled magnon propagation in $\text{Pt}/\text{Y}_3\text{Fe}_5\text{O}_{12}$ heterostructure, *Appl. Phys. Lett.* **117**, 152403 (2020).
- [4] A. Navabi, Y. Liu, P. Upadhyaya, K. Murata, F. Ebrahimi, G. Yu, B. Ma, Y. Rao, M. Yazdani, M. Montazeri, L. Pan, I. N. Krivorotov, I. Barsukov, Q. Yang, P. Khalili Amiri, Y. Tserkovnyak, and K. L. Wang, Control of spin-wave damping in YIG using spin currents from topological insulators, *Phys. Rev. Appl.* **11**, 034046 (2019).
- [5] K. S. Das, F. Feringa, M. Middelkamp, B. J. van Wees, and I. J. Vera-Marun, Modulation of magnon spin transport in a magnetic gate transistor, *Phys. Rev. B* **101**, 054436 (2020).
- [6] L. J. Cornelissen, J. Liu, B. J. van Wees, and R. A. Duine, Spin-current-controlled modulation of the magnon spin conductance in a three-terminal magnon transistor, *Phys. Rev. Lett.* **120**, 097702 (2018).
- [7] M. Evelt, V. E. Demidov, V. Bessonov, S. O. Demokritov, J. L. Prieto, M. Muñoz, J. Ben Youssef, V. V. Naletov, G. de Loubens, O. Klein, M. Collet, K. Garcia-Hernandez, P. Bortolotti, V. Cros, and A. Anane, High-efficiency control of spin-wave propagation in ultra-thin yttrium iron garnet by the spin-orbit torque, *Appl. Phys. Lett.* **108**, 172406 (2016).
- [8] G. Gubbiotti, S. Tacchi, M. Madami, G. Carlotti, A. O. Adeyeye, and M. Kostylev, Brillouin light scattering studies of planar metallic magnonic crystals, *J. Phys. D: Appl. Phys.* **43**, 264003 (2010).
- [9] J. Han, Y. Fan, B. C. McGoldrick, J. Finley, J. T. Hou, P. Zhang, and L. Liu, Nonreciprocal transmission of incoherent magnons with asymmetric diffusion length, *Nano Lett.* **21**, 7037 (2021). pMID: 34374550..
- [10] A. V. Sadovnikov, A. A. Grachev, S. E. Sheshukova, Y. P. Sharaevskii, A. A. Serdobintsev, D. M. Mitin, and S. A. Nikitov, Magnon straintronics: Reconfigurable spin-wave routing in strain-controlled bilateral magnetic stripes, *Phys. Rev. Lett.* **120**, 257203 (2018).
- [11] P. Pirro, V. I. Vasyuchka, A. A. Serga, and B. Hillebrands, Advances in coherent magnonics, *Nat. Rev. Mater.* **6**, 00332 (2021).
- [12] A. V. Chumak, V. Vasyuchka, A. Serga, and B. Hillebrands, Magnon spintronics, *Nature Phys.* **11**, 3347 (2015).
- [13] G. Csaba, Ádám Papp, and W. Porod, Perspectives of using spin waves for computing and signal processing, *Phys. Lett. A* **381**, 1471 (2017).
- [14] A. A. Serga, A. V. Chumak, and B. Hillebrands, YIG magnonics, *J. Phys. D* **43**, 264002 (2010).
- [15] A. Barman, *et al.*, The 2021 magnonics roadmap, *J. Phys.: Condens. Matter* **33**, 413001 (2021).
- [16] A. V. Chumak, T. Neumann, A. A. Serga, B. Hillebrands, and M. P. Kostylev, A current-controlled, dynamic magnonic crystal, *J. Phys. D: Appl. Phys.* **42**, 205005 (2009).
- [17] S. Mansfeld, J. Topp, K. Martens, J. N. Toedt, W. Hansen, D. Heitmann, and S. Mendach, Spin wave diffraction and perfect imaging of a grating, *Phys. Rev. Lett.* **108**, 047204 (2012).
- [18] J. Stigloher, M. Decker, H. S. Körner, K. Tanabe, T. Moriyama, T. Taniguchi, H. Hata, M. Madami, G. Gubbiotti, K. Kobayashi, T. Ono, and C. H. Back, Snell's law for spin waves, *Phys. Rev. Lett.* **117**, 037204 (2016).
- [19] J. Gräfe, P. Gruszecki, M. Zelent, M. Decker, K. Keskinbora, M. Noske, P. Gawronski, H. Stoll, M. Weigand, M. Krawczyk, C. H. Back, E. J. Goering, and G. Schütz, Direct observation of spin-wave focusing by a Fresnel lens, *Phys. Rev. B* **102**, 024420 (2020).
- [20] C. Y. Guo, C. H. Wan, M. K. Zhao, H. Wu, C. Fang, Z. R. Yan, J. F. Feng, H. F. Liu, and X. F. Han, Spin-orbit torque switching in perpendicular $\text{Y}_3\text{Fe}_5\text{O}_{12}/\text{Pt}$ bilayer, *Appl. Phys. Lett.* **114**, 192409 (2019).
- [21] C. Y. Guo, C. H. Wan, W. Q. He, M. K. Zhao, Z. R. Yan, Y. W. Xing, X. Wang, P. Tang, Y. Z. Liu, S. Zhang, Y. W. Liu, and X. F. Han, A nonlocal spin Hall magnetoresistance in a platinum layer deposited on a magnon junction, *Nat. Electron.* **3**, 304 (2020).
- [22] H. Wu, L. Huang, C. Fang, B. S. Yang, C. H. Wan, G. Q. Yu, J. F. Feng, H. X. Wei, and X. F. Han, Magnon valve effect between two magnetic insulators, *Phys. Rev. Lett.* **120**, 097205 (2018).
- [23] H. Wang, J. Chen, T. Liu, J. Zhang, K. Baumgaertl, C. Guo, Y. Li, C. Liu, P. Che, S. Tu, S. Liu, P. Gao, X. Han, D. Yu, M. Wu, D. Grundler, and H.

- Yu, Chiral spin-wave velocities induced by all-garnet interfacial Dzyaloshinskii-Moriya interaction in ultrathin yttrium iron garnet films, *Phys. Rev. Lett.* **124**, 027203 (2020).
- [24] X. Zhang, W. Li, M. Irfan, S. Parajuli, J. Wei, Z. Yan, X. Wang, N. Ahmad, J. Feng, G. Yu, and X. Han, Fabrication and characterization of YIG nanotubes, *J. Magn. Magn. Mater.* **482**, 358 (2019).
- [25] B. A. Kalinikos and A. N. Slavin, Theory of dipole-exchange spin wave spectrum for ferromagnetic films with mixed exchange boundary conditions, *J. Phys. C* **19**, 7013 (1986).
- [26] H. Qin, S. J. Hämäläinen, K. Arjas, J. Witteveen, and S. van Dijken, Propagating spin waves in nanometer-thick yttrium iron garnet films: Dependence on wave vector, magnetic field strength, and angle, *Phys. Rev. B* **98**, 224422 (2018).
- [27] J. R. Eshbach and R. W. Damon, Surface magnetostatic modes and surface spin waves, *Phys. Rev.* **118**, 1208 (1960).
- [28] H. Yu, O. d'Allivy Kelly, V. Cros, R. Bernard, P. Bortolotti, A. Anane, F. Brandl, R. Huber, I. Stasinopoulos, and D. Grundler, Magnetic thin-film insulator with ultra-low spin wave damping for coherent nanomagnonics, *Sci. Rep.* **4**, 6848 (2014).
- [29] O. Dzyapko, I. V. Borisenko, V. E. Demidov, W. Pernice, and S. O. Demokritov, Reconfigurable heat-induced spin wave lenses, *Appl. Phys. Lett.* **109**, 232407 (2016).
- [30] T. Wolfram and R. DeWames, Surface dynamics of magnetic materials, *Prog. Surf. Sci.* **2**, 233 (1972).